Applied Catalysis O: Open 194 (2024) 206997

Contents lists available at ScienceDirect

Applied Catalysis O: Open

journal homepage: www.elsevier.com/locate/apcato

Precise design and construction of NiO-Ni heterostructures for active hydrogen evolution photocatalysis

Khaja Mohaideen Kamal [a,*], Rekha Narayan [d], Selvakannan Periasamy [b], Sašo Gyergyek [c], Stefan Popović [d], Nejc Hodnik [d], Hsin-Chia Ho [f], Petar Djinović [e], Blaž Likozar [a,*]

[a] Department of Catalysis and Chemical Reaction Engineering, National Institute of Chemistry, 1001 Ljubljana, Slovenia
[b] Centre for Advanced Materials and Industrial Chemistry (CAMIC), School of Applied Sciences, RMIT University, Melbourne 3001, Australia
[c] Department for Materials Synthesis, Jožef Stefan Institute, Jamova 39, SI-1000 Ljubljana, Slovenia
[d] Department of Materials Chemistry, National Institute of Chemistry, 1001 Ljubljana, Slovenia
[e] Department of Inorganic Chemistry and Technology, National Institute of Chemistry, 1001 Ljubljana, Slovenia
[f] Advanced Materials Department, Jožef Stefan Institute, Jamova Cesta 39, 1000 Ljubljana, Slovenia

ARTICLE INFO

Keywords:
Photocatalytic H_2 evolution
Interface
Metallic Ni
NiO
Hot electron transfer

ABSTRACT

The design of metal-oxide-metal heterostructure photocatalysts is an effective and widely used approach to solve global environmental problems. In this work, we designed and prepared a NiO-rich NiO-Ni heterostructure in an N-doped carbon matrix as a photocatalyst using a simple chemical method for hydrogen evolution reactions. It has an optimal photocatalytic hydrogen production rate of 1395 μmol. g^{-1}. h^{-1}, which is ~8 times higher than that of Ni rich NiO-Ni (178 μmol. g^{-1}. h^{-1}). Combined experimental results demonstrate that such a good performance benefits from the specific NiO-Ni interface, which could improve the utilization of sunlight and charge separation efficiency. Moreover, this interface contributes to improved structural stability during the photocatalytic reactions, ensuring superior catalytic performance. This work provides a new strategy for the design and synthesis of efficient precious-metal-free heterostructure catalysts for photocatalytic hydrogen evolution reactions.

1. Introduction

Hydrogen (H_2) has been regarded as a promising green and sustainable energy source, offering an attractive alternative to traditional fossil fuels [1–3]. Compared with conventional H_2 production technology, photocatalytic hydrogen evolution reaction (HER) is an environmentally friendly route that is of great importance for new energy utilization and environmental protection [4–7]. Several strategies have been employed to enhance the photocatalytic efficiency, including defect engineering, heterostructure construction with other semiconductors, nanostructure formation, and metal doping [8–11]. In order to meet the specific needs of overall water splitting, such as having an appropriate band gap, being able to separate and transfer photogenerated electron-hole (e-h) pairs, being stable against photocorrosion, and having a fast reaction rate, a wide range of catalysts are currently being researched [12,13]. The most effective catalysts for HER are those based on platinum (Pt), however their greater cost and scarcity make them unfeasible for widespread use in HER [14]. As a result, for photocatalytic hydrogen evolution, the creation of an effective and affordable semiconductor catalyst based on non-precious metals is essential.

Non-noble 3d transition metals, like nickel (Ni), have been seen as viable substitutes for Pt in HER, particularly in alkaline environments [15]. In the meantime, it has been demonstrated that metal oxides can quicken the water dissociation process. Compared to pure metals, metal oxide/metal heterojunction-like structures exhibit increased HER activity. Strmčnik and associates stated that under alkaline conditions, the dissociation of H_2O is a necessary step for HER and that metal-metal oxide is a significant factor in the dissociation of water [16,17]. The primary explanation for the enhanced catalytic performance toward the HER has been proposed to be a synergistic electronic interaction between the metal and the oxide. Since NiO has a strong affinity for the formation of adsorbed hydroxyl species, or OH_{ads}, and H adsorption on metallic Ni is preferred, NiO-Ni catalysts may hold the key to the development of robust, active, and inexpensive catalysts. According to research team Wang Yong, enhanced catalytic performance depends on

* Corresponding authors.
E-mail addresses: khaja.mohaideen.kamal.musthafa@ki.si (K.M. Kamal), blaz.likozar@ki.si (B. Likozar).

https://doi.org/10.1016/j.apcato.2024.206997
Received 17 May 2024; Received in revised form 16 July 2024; Accepted 26 July 2024
Available online 28 July 2024

the metallic Ni at the Ni-NiO interface [18]. Dong and others discovered that the enhanced HER performance at the Ni-NiO interface is caused by slightly oxidized Ni atoms rather than metallic Ni atoms [19]. Oshchepkov and associates discovered that the presence of NiO on the metallic Ni surface causes a tenfold increase in the catalytic activity of Ni [20]. Gong et al., demonstrated that while the HER activity of Ni/NiO core-shell heterostructures is comparable to that of Pt, it deactivates after 24 h [21]. NiO-Ni nanostructures have been mainly studied in the field of electrocatalytic HER and their application in the photocatalytic HER is very limited. It is still difficult to create a reliable catalytic system for photocatalytic HER based on the NiO-Ni interface.

This work presents the preparation of NiO-Ni heterostructure within a nitrogen doped carbon matrix using the Glycine-Nitrate-Process (GNP method) in order to enhance the light trapping performance, encourage electron separation from photogenerated charge carriers and decrease charge carrier recombination. Photocatalytic hydrogen evolution from water without a hole's sacrificial agent and co-catalysts are achieved.

2. Experimental section

2.1. Materials

All reagents were analytical grade and used with none further purification. Milli-Q water was used throughout the work.

2.2. Preparation of NiO, NiO rich NiO-Ni and Ni rich NiO-Ni catalysts

Various nickel catalysts with different oxidation states were prepared by GNP method [22,23]. Typically, 1 mol of nickel nitrate, Ni $(NO_3)_2.6H_2O$ (Aldrich) was dissolved in a 10 mL of distilled water. Glycine (Aldrich), corresponding to different glycine to nitrate ratios (Glycine/Nitrate (G/N) ratios = 0.5, 1 and 2), was also dissolved separately in a 10 mL of distilled water. All the solutions (nickel nitrate and glycine) were mixed thoroughly by ultrasonicating for 2 min. The mixed solution was then transferred to a crystallizing dish and the dish with its contents was subjected to heating on a laboratory hot plate at a temperature of about 200 °C. After complete evaporation of water, the resulting viscous liquid ignited automatically giving rise to a fluffy mass. This procedure was repeated for different G/N ratios. For convenience, the as-synthesized catalysts are coded as GN-0.5 (NiO), GN-1 (NiO rich NiO-Ni) and GN-2 (Ni rich NiO-Ni), respectively.

2.3. Material characterizations

X-ray diffraction (XRD) was performed using an X'Pert MPD diffractometer (PANalytical) with Cu Kα radiation, in the 2θ range from 20° to 90°, and using JCPDS database for reference. Transmission electron microscopy (TEM) was performed at 200 kV with a thermionic electron-source on a JEOL JEM-2100. Magnetizations (M) versus field (H) measurements were made at room temperature up to a maximum field of 10 kOe on a LakeShore vibrating sample magnetometer 7404 VSM. The Brunauer-Emmett-Teller specific surface area (S_{BET}), Pore Volume (V_{pore}) and Pore Diameter (D_{pore}) were determined from N_2 adsorption-desorption isotherms obtained at −196 °C (ASAP 2020, Micromeritics, USA). The optical properties of the samples were analyzed using a UV–Vis-DRS spectrophotometer (Perkin Elmer). The Raman spectrum was obtained from a Raman microscope (Witec Alpha 300 RA) in the spectral range from 3600 cm^{-1} to 70 cm^{-1}, using a green laser with the excitation wavelength of 532 nm. X-ray photoelectron spectroscopy (XPS) was obtained from a Thermo Scientific K-Alpha instrument (monochromatic Al K_α radiation, E_{photon} = 1486.6 eV). The binding energy (B.E) in each case, that is, core levels and valence band maxima were corrected using an internal reference peak of C 1 s peak centered at 284.8 eV. Photoluminescence (PL) spectra of the sample-water suspensions (1 mg mL^{-1}) were recorded with a Synergy H1 microplate reader with monochromator optics (Bio-Tek, USA) at an excitation wavelength of 300 nm in 96-well microplates (Nunc) using the top optics.

2.4. Photoelectrochemical measurements

All photoelectrochemical (PEC) measurements, impedance, Mott-Schottky, and photocurrent response measurements were assessed in a 0.5 M Sodium sulfate (Na_2SO_4) aqueous solution after being bubbled with N_2 gas for 30 min. The PEC measurements were carried out using a standard three-electrode glass cell on potentiostat/galvanostat (Biologic SP 200). A Pt rod and Ag/AgCl were used as the counter and reference electrodes, respectively. The sample coated on Fluorine-doped tin oxide (FTO) glass was used as the working electrode. A 300 W Xenon lamp was used as the light source during PEC measurements, which ensured that the effective irradiation area on the samples was 1.5 cm^2. The potentiostatic electrochemical impedance spectra's (PEIS) were recorded at an open-circuit voltage (OCV) within the frequency range of 100 kHz to 10 Hz with an ac amplitude of 10 mV. Manual internal resistance (MIR) was employed to compensate for the 85% resistance of the electrolyte. Photocurrent response tests were carried out with applied bias of −0.3 V vs. Ag/AgCl and periodic 20s of illumination within 20s of light-off as relaxation period in-between. Each experiment was performed in a total of 180 s. Mott-Schottky measurements were performed using a standard three-electrode glass cell with potentiostat/galvanostat (Biologic SP 200) with the same electrodes as for photocurrent response tests to determine the flat band energy position. Linear sweep voltammetry (LSV) was performed at −1.0 V to 0 V at a scan rate of 5 $mV.s^{-1}$.

2.5. Photocatalytic hydrogen production test

The photocatalytic H_2 evolution reactions (HER) were carried out in a 80 ml quartz round bottom flask at ambient temperature and atmospheric pressure using mixing to achieve particle suspension. A commercial solar simulator equipped with a Xenon arc lamp (300 W, Newport) was used as a light source, as illustrated in Fig. S2. For pH 7, the phosphate buffer solution was made using the Henderson-Hasselbalch Eq. [24]. In short, 42.2 ml of 0.1 M KH_2PO_4 and 57.8 ml of 0.1 M K_2HPO_4 were mixed together to obtain 100 ml phosphate buffer solution of pH 7. In a typical photocatalytic experiment, 20 mg of photocatalyst was suspended in 50 ml of phosphate buffer solution and the suspension was sonicated for 30 min to obtain well-dispersed particle suspension. Before the light irradiation, the quartz flask was sealed with rubber septum and purged with nitrogen flow for 30 min to remove all oxygen. Eventually, the sealed flask was placed under light illumination. All the photocatalysts were subjected to 3 h light irradiation and H_2 evolution was measured every hour periodically. The generated gas composition was analyzed with a gas chromatography (GC, SRI—8610C) equipped with thermal conductivity detector (TCD) and high purity nitrogen was used as carrier gas.

The apparent quantum efficiency (AQE) was a significant piece of evidence to evaluate the utilization factor of the solar light, and this was calculated based on the following Eq. [25].

$$\text{AQE}\ (\%) = \frac{\text{Number of reacted electrons}}{\textit{Number of incident photons}} \times 100$$

3. Results and discussion

3.1. Structural analysis of the catalysts

The X-ray diffraction (XRD) patterns of G/N-0.5, G/N-1, and G/N-2 are shown in Fig. 1b. For G/N-0.5, the diffraction lines at 37.0, 43.1, 62.6, 75.0, and 79.0° belong to the (111), (200), (220), (311), and (222) planes of cubic nickel oxide, NiO (JCPDS: 01–089-7130). On the other hand, along with NiO, reflections from metallic Ni are seen in case of G/N-1, indicating that metallic Ni was in situ generated. The G/N-2

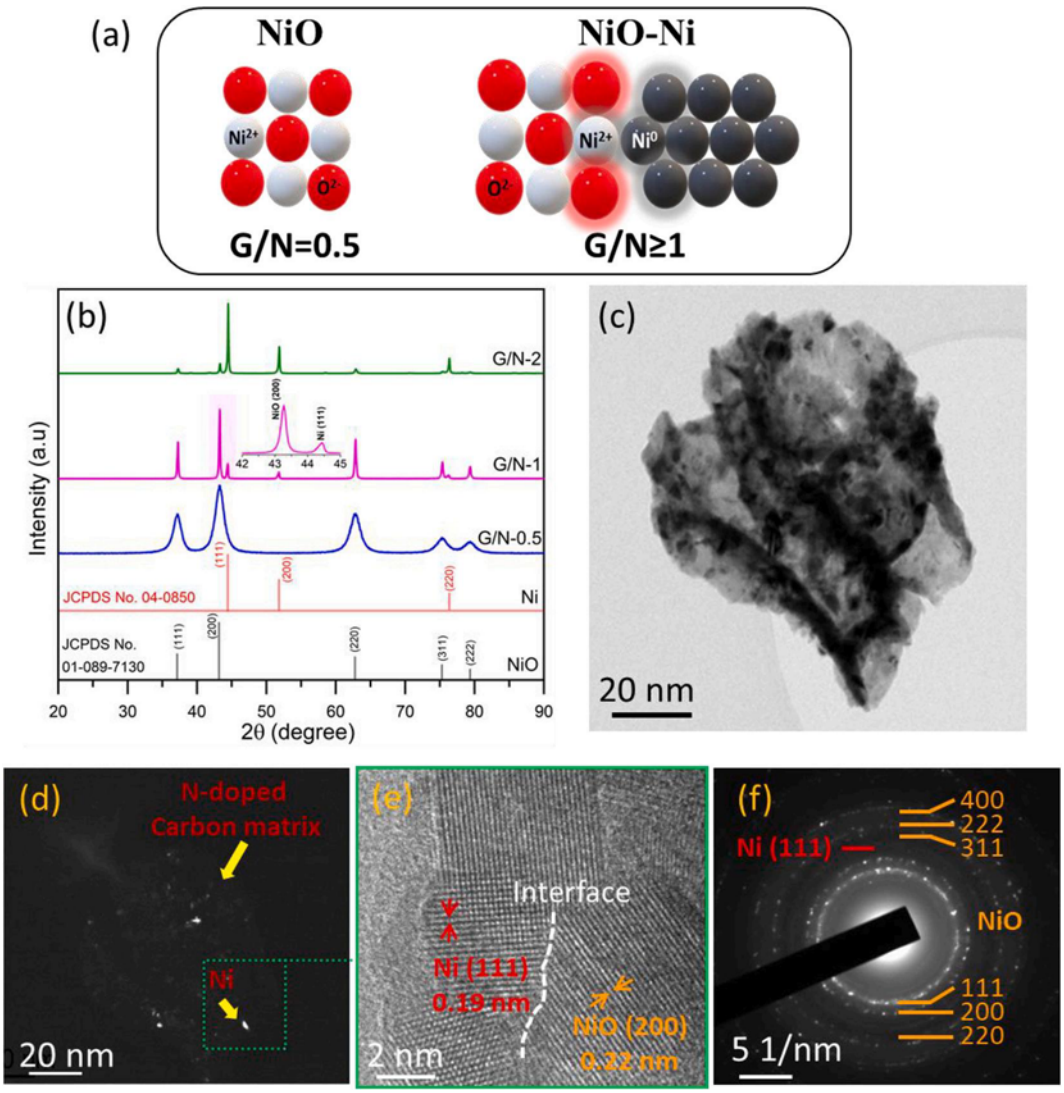

Fig. 1. (a) Schematic diagram of the synthesis method of NiO and NiO-Ni catalysts from different G/N ratios. (b) Comparison of XRD patterns of as-prepared samples. TEM images of G/N-1 (c-d) bright and dark-field image of the same region acquired by the Ni(111) reflection (e) high-resolution TEM visualization of the G/N-1 with NiO-Ni interface and (f) SAED pattern of NiO and Ni.

samples corresponding to the (111), (200), and (222) planes of metallic Ni (JCPDS: 04–0850) exhibited distinct peaks at 44.5, 51.8, and 76.4°. Thus, XRD studies make it clear that the present GNP method gives metal oxide/metal nanocomposites when the appropriate G/N ratios are used during the combustion reaction. A detailed morphological study of the G/N-1 sample was performed by transmission electron microscopy (TEM) and high-resolution TEM (HRTEM), as shown in Fig. 1c-e, which demonstrates that, the sample consists of assembled nanostructures. Furthermore, interfaces between NiO and Ni in many particles could also be clearly seen by HRTEM (Fig. 1e). The well-resolved lattice spacings of 0.19 nm and 0.22 nm, respectively, were clearly consistent with the (111) crystal plane of metallic Ni and the (200) crystal plane of NiO, which is in good agreement with the powder XRD patterns. Selected Area Electron Diffraction (SAED) pattern depicted in Fig. 1f is made up of bright rings that closely matched the nanostructures of NiO and Ni, further proving the heterogeneous structure and interface interaction of the NiO and Ni. Nitrogen adsorption/desorption isotherms and pore size distributions were measured to further characterize the structure of samples G/N-0.5, G/N-1 and G/N-2 (Fig. S1 and Table S1). With increasing Ni content, the specific BET surface areas decrease from 30 (G/N-0.5) to 6 (G/N-1) and to 5 (G/N-2). This is plausible since the agglomerated larger Ni particles have smaller specific surface areas than the pure NiO. The pore size distribution diagram (Fig. S1, inset figure) shows that all catalysts have a narrow pore size distribution with an average pore diameter of ~3–4 nm, calculated by the BJH method. The nitrogen physisorption experiments of the catalysts resulted in type IV isotherms, a property of mesoporous materials [26]. The mesoporous structure is helpful for the catalytic performance.

X-ray photoelectron spectroscopy (XPS) was used to ascertain the surface oxidation states and chemical composition of the as-prepared catalysts. Fig. 2a displays the sample's wide range XPS spectrum and demonstrates the elements Ni, O, N, and C's presence. As depicted in Fig. 2b, Ni 2p consists of two spin orbit doublets, which are characteristic peaks of Ni^{2+}/Ni^{0} and two satellite peaks. Ni—Ni bonding is responsible for the deconvoluted peaks of Ni $2p_{3/2}$ and Ni $2p_{1/2}$, and the dominance of NiO is indicated by their binding energy difference of ~17.70 eV. The deconvoluted peaks at binding energies of 853.63 eV and 855.42 eV are attributed to Ni $2p_{3/2}$, while the broad satellite peaks at 860.55 eV and 879.05 eV strongly suggest the formation of a NiO-Ni heterojunction on the surface of G/N-1 and G/N-2. The peaks at 871.18 eV and 873.53 eV are due to Ni $2p_{1/2}$, which can be assigned to metallic Ni and metal oxide NiO. The results indicate that as the glycine content increases, the amount of metallic Ni vacancies increases while the intensity of the characteristic Ni peak increases. As can be seen in the O 1 s

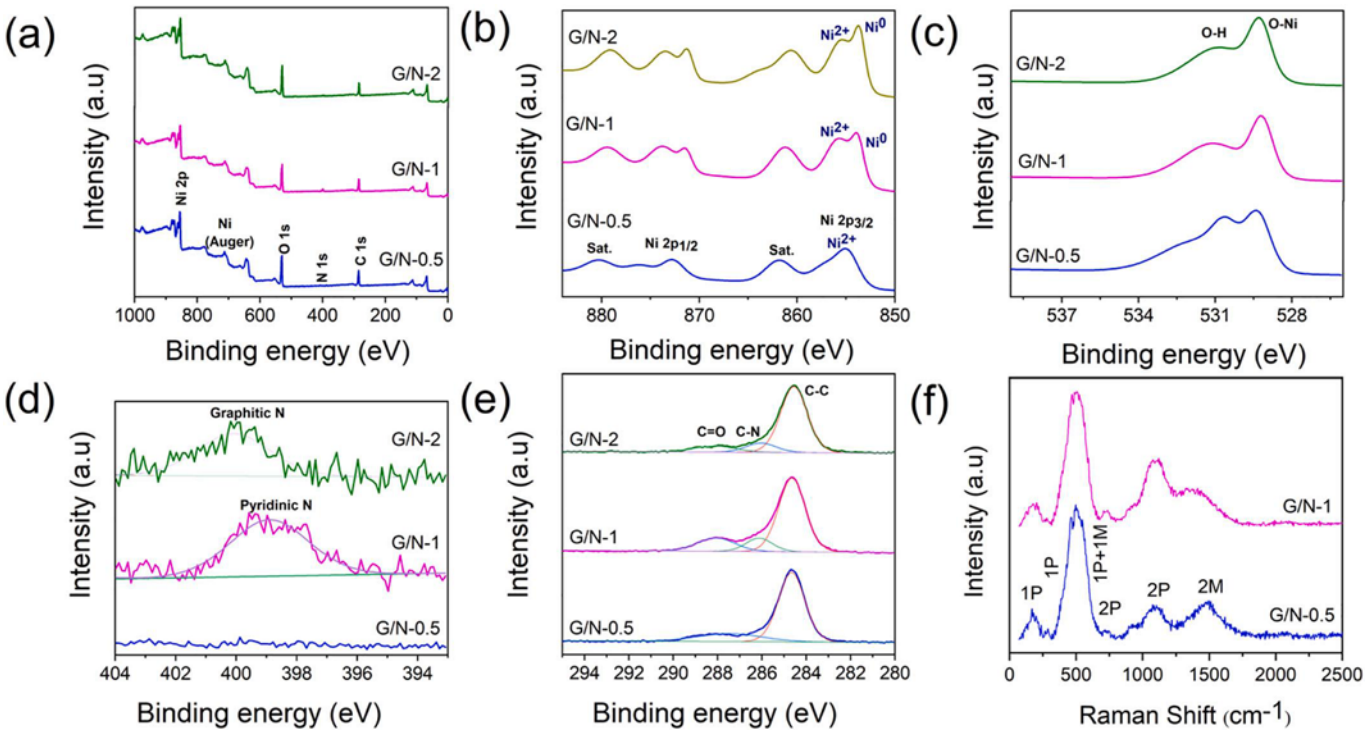

Fig. 2. XPS spectra (a) survey spectrum (b) Ni 2p (c) O 1 s (d) N 1 s (e) C 1 s and (f) Raman spectra of as-prepared samples.

spectrum in Fig. 2c, the two peaks can be mainly attributed to the metal-oxygen bond (529.23 eV), and the O—H species (531.14 eV), respectively. As shown in Fig. 2d, the N—C bonds in the samples of G/N-1 and G/N-2 are in the form of pyridinic N (398.9 eV) and graphitic N (400.9 eV), while G/N-0.5 has no peaks in the same binding energy range. Quantitative analysis of the XPS results shows that the atomic ratios of N/C in G/N-0.5, G/N-1 and G/N-2 are 0%, 3.24%, and 5.34%, respectively. It is noteworthy that the N/C content gradually increases with increasing glycine content. The presence of N dopants in the composites would increase the ability to interact with reactants and cause high positive charge density on their neighbouring carbon atoms, which could also contribute to the high activity of the G/N samples. The C 1 s spectrum of G/N-1 shown in Fig. 2e, the peaks representing C—C at 284.6 eV, C—N at 286.0 eV, and C═O at 288.0 eV. This could be because of the strong interaction between NiO and the N-doped carbon matrix [27–30]. Additional evidence from Raman analysis reconfirmed the existence of NiO in the G/N samples (Fig. 2f) while the G/N-2 demonstrated no peaks in the same region. Raman spectra revealed five unique peaks at 200, 520, 729, 1106, and 1500 cm^{-1}. The longitudinal optical (LO) one phonon (1P) band could be identified by the Raman spectral peak at approximately 200 cm^{-1} and 520 cm^{-1}. The two-phonon (2P) excitation in the 2TO mode was responsible for the peak at 729 cm^{-1}, the TO+LO mode was identified by the peak at 890 cm^{-1}, and the longitudinal optical (2LO) two phonon (2P) band was identified by the broad peak at 1106 cm^{-1}. These peaks may correspond to the Ni—O bond vibrational bands. It's interesting to note that the two-phonon band at approximately 1100 cm^{-1} in the G/N-1 sample was more intense than the two-magnon (2 M) band at approximately 1500 cm^{-1}. This difference in intensity could be explained by the presence of a metallic Ni phase that contributes to a high hole concentration [31–33].

3.2. Magnetic properties

The magnetic characteristics of GN series samples were measured using a vibrating sample magnetometer (VSM), with an applied magnetic field between −10 kOe to 10 kOe. Room temperature magnetic measurements on the as-synthesized powder samples are shown in Fig. 3. Magnetic hysteresis loop was not observed for G/N-0.5 suggesting that their magnetic moments were low. The magnetization was found to be saturated and the saturation magnetization (Ms) were determined to be 4.90 emu. g^{-1} and 31.8 emu. g^{-1}, for the samples G/N-1 and G/N-2, respectively and there was also a corresponding variation of the coercivity (Table S1). Based on results from the magnetic properties, we can find that the magnetization and coercivity of GN samples are ascribed to the generation of magnetic Ni nanoparticles [34]. Therefore, the large difference in the value of saturation magnetization indicates the various contents of metallic Ni in the obtained GN samples. In other words, the as-prepared GN samples present the gradually enhanced metallic Ni content with increasing the G/N ratios from 0.5 to 2.

3.3. Photocatalytic performance

All tested samples exhibit H_2 production activity except G/N-0.5, indicating the rapid recombination of photogenerated charges in pure NiO, while photocatalysts G/N-1 and G/N-2 exhibit 4185 and 534 μmol. g^{-1} H_2 for 3 h under full spectrum illumination (Fig. 4a). The H_2 evolution rates of all photocatalysts are summarized in Fig. 4b. The improved photocatalytic performance of G/N-1 is likely due to the accelerated photocarrier separation caused by metallic Ni acting as an electrons trap. Further, the introduction of metallic Ni into the metal oxide NiO led to a significantly increased enhanced photocatalytic HER activity. The H_2 evolution rate of G/N-1 increased with increasing the mass ratio of G/N. When the mass ratio of G/N reaches 1.0 (metallic Ni content: 9.9%), the H_2 evolution rate reaches the highest value of 1395 μmol.g^{-1}.h^{-1}, which is roughly eight times larger than that of G/N-2, suggesting that excessive G/N ratio increases the relative content of metallic Ni (70.3%) in G/N-2, which reduces the abundance of active sites and HER efficiency. Consequently, increasing the activity of photocatalysts requires proper G/N ratios. Next, by fitting the Xenon lamp with various bandpass filters, the photocatalytic HER activity of G/N-1 was examined under various irradiation circumstances. The apparent quantum efficiencies (AQEs) of the G/N-1 sample at 360, 400, and 420

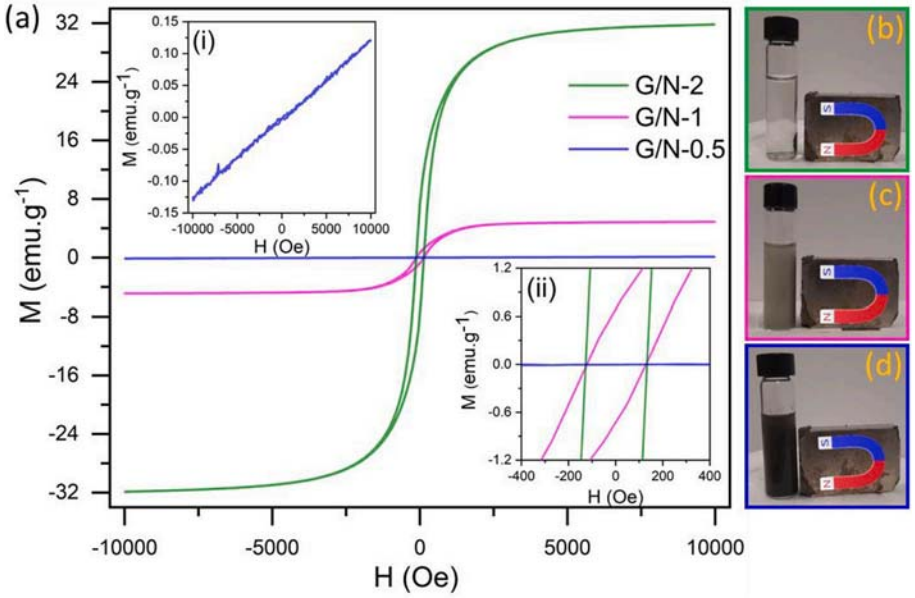

Fig. 3. (a) Room temperature M vs H curves of the as-synthesized powder samples. The corresponding insets show enlarged M-H curve of G/N-0.5 (i) and magnified view of M-H curves (ii). (b-d) Photograph of a vial with G/N-2, G/N-1 and G/N-0.5 samples in contact with a magnet, respectively.

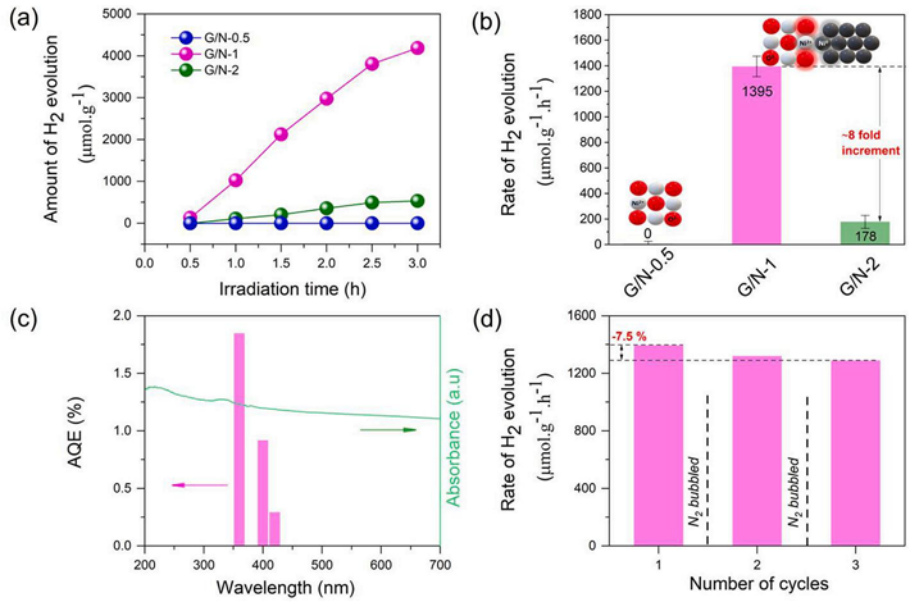

Fig. 4. (a) The time course of photocatalytic HER activity over G/N-0.5, G/N-1 and G/N-2 under full-spectrum light. (b) Their corresponding photocatalytic HER rates. (c) The wavelength-dependent AQE of photocatalytic HER over G/N-1. (d) The repeated cycles of photocatalytic HER rates of G/N-1. Photocatalytic reaction conditions: pH = 7 phosphate buffer solution (50 mL), catalyst (20 mg), irradiation time (3 h), Room temperature, atmospheric pressure and 300 W Xenon lamp.

nm were measured to be 1.850, 0.919, and 0.295, respectively (Fig. 4c). As the wavelength increases, the AQE gradually decreases, which is consistent with the trend of the UV–vis-DRS absorption spectrum of G/N-1, indicating that the HER reaction is indeed initiated by light excitation of the photocatalyst. Control experiments were performed in the dark, and no H_2 was released, showing that the HER reaction is a photon-driven process (Fig. S3, ESI†). The blank reaction without any catalyst was carried out and it showed that no H_2 was produced, indicating that the HER reaction is catalyzed by photocatalyst. Photostability is another important factor for evaluating the performance of photocatalysts. Fig. 4d and Fig. S5 (ESI†) compare the photoactivities of the G/N-1 and G/N-2 samples after three cycles (3 h in one cycle) reactions. A slight decrease in the photocatalytic H_2 production rate of G/N-1 (7.5%) could be observed after three cycles, while that of the G/N-2 dropped significantly by 89.7%. The XRD data, TEM and SEM images of the G/N-1 sample before and after the stability test are shown in Fig. S6 and Fig. S7 (ESI†). A comparison of the XRD, TEM and SEM between fresh and used GN-1 samples shows that the NiO-rich NiO-Ni is not aggregated during the reaction process, indicating good stability. Those results show that the hierarchical NiO-Ni interface dramatically increases both the H_2 evolution activity, photochemical and structural stability. The catalytic activity of our G/N-1 catalyst also shows superior performance compared to other previously reported Ni-based photocatalysts (see Table S4, Supplementary Information).

3.4. Optical and electronic properties and photocatalytic mechanism

It can be seen from Fig. 5a that G/N-1 and G/N-2 exhibits a higher absorption in the wavelength range of 200–850 nm compared to G/N-0.5. With an increase in Ni content, the range of light absorption can be expanded from the UV to the visible, indicating that metallic Ni can effectively enhance the light absorption of the NiO-Ni composite. This composite can then function as a heterojunction component to improve light utilization at the NiO-Ni interface. In addition, the band gap values of 2.80 (G/N-0.5), 2.60 (G/N-1) and 2.45 (G/N-2) can be obtained via the linear fit in Fig. 5b. As illustrated in Fig.5c, the Photoluminescence (PL) spectrum of G/N-0.5 exhibits a prominent peak at 385 nm. This emission is caused by the excitonic recombination of electrons in the conduction band with holes in the valence band of NiO, which occurs close to the band edge. This outcome is in good agreement with earlier reports on the PL of NiO [35,36]. Specifically, the PL intensity of the G/N-1 and G/N-2 catalysts was much lower, indicating that an increase in Ni metal content improved the separation efficiency of the photo-generated charge carriers.

Based on the photoelectrochemical characteristics of the produced photocatalysts, the transfer and separation of charge carriers are studied. As revealed in Fig. 5d, the photocurrent response of the G/N-1 sample is remarkably improved as compared to those of the bare G/N-0.5 and G/N-2 samples, shows that the NiO-Ni interface remarkably boosted the charge separation. It is worth mentioning that the photo-response signals during the on-off cycles were highly reproducible, indicating the structural and chemical stability of the tested samples. The EIS method was used to examine the interfacial photophysical properties of the prepared samples (Fig. 5e). The order of G/N-1 < G/N-2 < G/N-0.5 is followed by the arc radius of the EIS-Nyquist plot, indicating that the interface between the semiconducting metal oxide and transition metal can improve the efficiency of charge carrier separation. To further confirm the above results, Fig. S8 shows the linear sweep voltammetry (LSV) curves of samples G/N-0.5, G/N-1 and G/N-2. The G/N-1 shows the lowest overpotential of ~0.83 V (vs reversible hydrogen electrode, RHE) at a current density of 10 mA.cm^{-2}, suggesting that the formation of G/N-1 systems could significantly promote the reduction of protons to H_2. Together with the photoelectrochemical measurements and catalytic activity, the G/N-1 hybrids can be promising photocatalysts available for efficient proton reduction for H_2 production. These findings show that NiO-Ni interfaces significantly improve electron-hole pair separation and collection efficiency, which in turn promotes an increase in the HER activity.

The flat band potential (E_{fb}) of the semiconducting material is obtained by the nodal increment of the fitting a regular line at $C^{-2} = 0$. As shown in Fig. 5f and g, the E_{fb} at 1.90, 0.75 and − 1.03 V for G/N-0.5, G/N-1 and G/N-2 (vs. Ag/AgCl) are determined by the Mott-Schottky (M-S) formula, which are converted to 2.10, 0.95 and − 0.83 V (vs. NHE), respectively. G/N-0.5 and G/N-1 are shown to have a negative slope in the Mott-Schottky plots, while G/N-2 has a positive slope. These results suggest that G/N-0.5 and G/N-1 are p-type semiconductors, while G/N-2 is an n-type semiconductor. The flat-band potential (the X-intercept) of p-type semiconductors is 0.2 eV greater than the valence band edge (E_{VB}) potential, whereas the flat-band potential (the X-intercept) of n-type semiconductors is 0.2 V greater than the conduction band edge (E_{CB}) [37–39]. As a result, it was established that the final E_{VB} positions for G/N-0.5, G/N-1, and G/N-2 were 2.30, 1.15, and 1.42 V vs NHE, respectively. Next, using the formula $E_{CB} = E_{VB}$-E_g, the E_{CB} of G/N-0.5, G/N-1, and G/N-2 were determined to be −0.5, −1.45, and − 1.03 V, respectively [40].

As illustrated in Fig. 6a, the CB position of as-obtained G/N-1 upshifts 0.42 V than the G/N-2 sample, which represents the improved thermodynamic driving force for photocatalytic proton reduction. A potential reaction mechanism for the photocatalytic process is suggested below, based on the analyses above: Ni nanoparticles use the surface plasmon resonance (SPR) effect to produce hot electrons when exposed

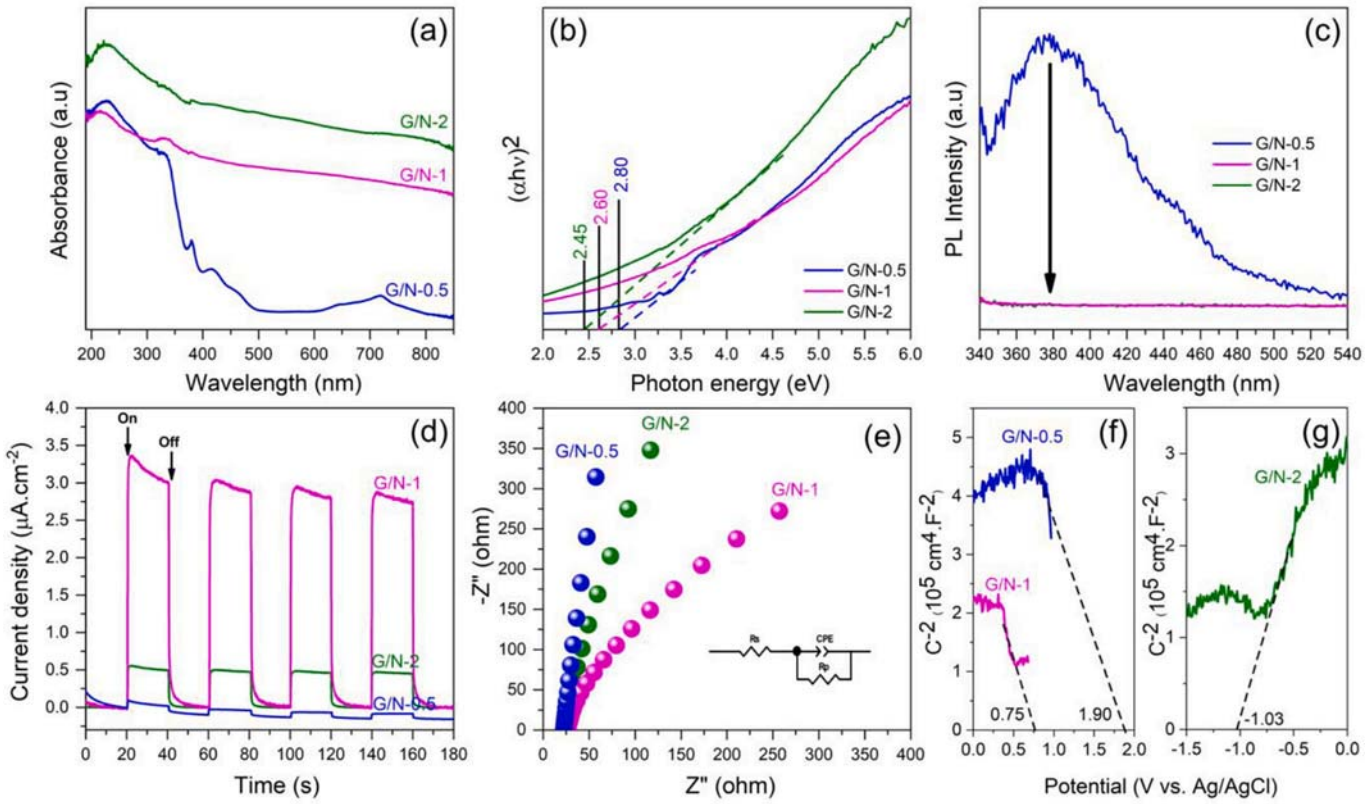

Fig. 5. (a) UV–vis-DRS spectra and (b) Tauc's plots (c) Photoluminescence spectra (d) Transient photocurrent response (TPCR) curves (e) Nyquist plots (f-g) Mott-Schottky plots collected at 1300 Hz for the samples G/N-0.5, G/N-1 and G/N-2.

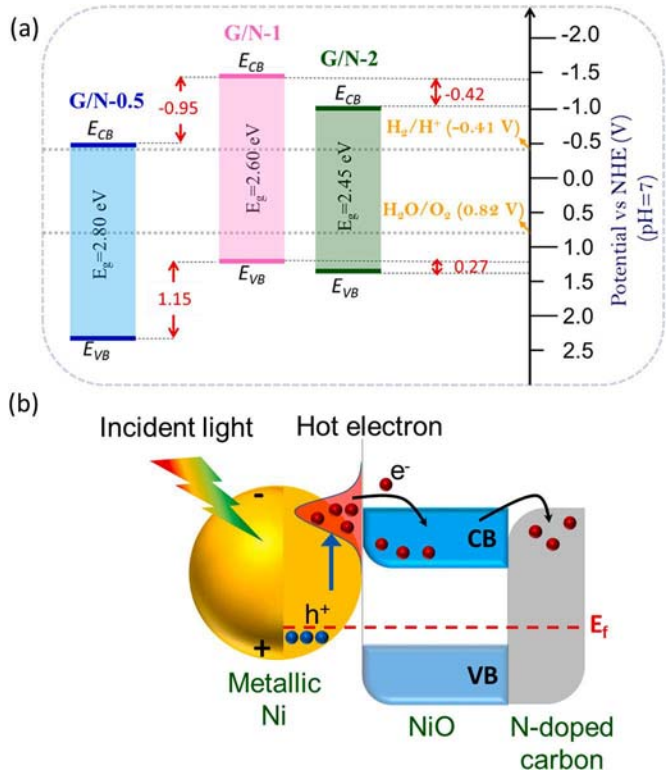

Fig. 6. (a) Schematic illustration of the energy band structure and (b) hot electron injection from metal NPs to the CB of semiconductor and N-doped carbon under light illumination.

to light. Furthermore, an interface or dielectric medium is needed for SPR. For Ni metal nanoparticles, NiO and the N-doped carbon matrix can function as a dielectric layer to promote surface plasmon generation. Fig. 6b shows the schematic of the underlying photocatalytic HER mechanism of the Ni-NiO/N-doped carbon matrix under light illumination. During H_2 production, hot charge carriers are transferred to the N-doped carbon matrix via the dielectric NiO layer in the first step. Furthermore, when a semiconductor is chemically bound to a plasmonic nanoparticle, it has been demonstrated that plasmon relaxation can happen by the direct and efficient, simultaneous excitation and transfer of e^- or h^+ from the metallic nanoparticle to the attached metal oxide semiconductor. In addition, the enhancement of charge carrier tunneling from the metal to the metal oxide semiconductor has been facilitated by the existence of a thin dielectric layer [41,42]. Because the surface of the NiO/N-doped carbon matrix comes into contact with H_2O, the (h^+) oxidizes H_2O and generates H^+. Then, the (e^-) reduces H^+ and gathers it at the conduction band (CB) of the shell to produce H_2. This can be explained by the active adsorption site that exists in the N-doped carbon matrix on the surface of the Ni-NiO/N-doped carbon matrix structure. Such a result is in good agreement with the metallic Ni-based catalyst's or co-catalyst's active and effective role in photocatalytic water splitting to produce hydrogen [43,44]. Taken together, all the above results certainly confirm that the NiO rich NiO-Ni within the N-doped carbon matrix is an active, selective, and stable catalyst for photocatalytic H_2 production.

4. Conclusions

The hierarchical NiO rich NiO-Ni heterostructure in a nitrogen doped carbon matrix was rationally designed and successfully demonstrated as an efficient photocatalyst for the HER. Systematic characterization confirms the existence of NiO and metallic Ni in the N-doped carbon matrix and supports their role in promoting charge separation and enhancing light absorption. The NiO rich NiO-Ni heterostructure (G/N-1) shows the highest H_2 evolution activity (1395 μmol. g^{-1}. h^{-1}) and it is ~8 times higher than the Ni rich NiO-Ni heterostructure (G/N-2). The interface between metal oxide and metal in the heterostructure, which encourages the transfer of photoinduced charge carriers from metallic Ni to NiO, is responsible for the increased HER activity. The findings also highlight how crucial it is for the N-doped carbon matrix to contain both Ni metal and oxide sites in order to achieve excellent and long-lasting HER performance using a simple synthesis process. This study provides novel perspectives for the exploration and design of high-performance photosynthesis components for solar energy conversion.

CRediT authorship contribution statement

Khaja Mohaideen Kamal: Writing – review & editing, Writing – original draft, Validation, Methodology, Investigation, Formal analysis, Data curation, Conceptualization. **Rekha Narayan:** Formal analysis, Data curation. **Selvakannan Periasamy:** Formal analysis, Data curation. **Sašo Gyergyek:** Formal analysis, Data curation. **Stefan Popović:** Formal analysis, Data curation. **Nejc Hodnik:** Formal analysis, Data curation. **Hsin-Chia Ho:** Formal analysis, Data curation. **Petar Djinović:** Formal analysis, Data curation. **Blaž Likozar:** Writing – review & editing, Validation, Supervision, Resources, Project administration, Investigation, Funding acquisition.

Declaration of competing interest

The authors declare that they have no known competing financial interests or personal relationships that could have appeared to influence the work reported in this paper.

Data availability

Data will be made available on request.

Acknowledgements

KKM and BL are gratefully acknowledging the funding from the EU commission for Horizon 2020 Framework Programme- Marie Skłodowska-Curie Individual Fellowship, Project-PhotoCatRed (grant agreement 841676), European climate, infrastructure and environment executive agency (CINEA) under grant agreement No. 101118129, Project: PHOTOSINT and European innovation council and SMES executive agency (EISMEA) under grant agreement No. 101046836, Project: CATART. SG acknowledges the financial support from the Slovenian Research Agency (research core funding No. P2-0089). NH and SP are grateful to the financial support from the core programme P2-0393 and projects J7-4636 and N2-0248.

Appendix A. Supplementary data

Supplementary data to this article can be found online at https://doi.org/10.1016/j.apcato.2024.206997.

References

[1] M.R. Kandel, U.N. Pan, P.P. Dhakal, R.B. Ghising, S. Sidra, D.H. Kim, N.H. Kim, J. H. Lee, Manganese-doped bimetallic $(Co,Ni)_2$ P integrated CoP in N,S Co−doped carbon: unveiling a compatible hybrid electrocatalyst for overall water splitting, Small 20 (2024) 2307241, https://doi.org/10.1002/smll.202307241.

[2] M.R. Kandel, U.N. Pan, P.P. Dhakal, R.B. Ghising, T.T. Nguyen, J. Zhao, N.H. Kim, J.H. Lee, Unique heterointerface engineering of Ni_2P−MnP nanosheets coupled Co_2P nanoflowers as hierarchical dual-functional electrocatalyst for highly proficient overall water-splitting, Appl. Catal. B 331 (2023) 122680, https://doi.org/10.1016/j.apcatb.2023.122680.

[3] U.N. Pan, M.R. Kandel, A.K. Tomar, N.H. Kim, J.H. Lee, Synchronous surface-interface and crystal-PhaseEngineered multifaceted hybrid nanostructure of Fe-(1T)-VSe_2 nanosheet and Fe-$CoSe_2$ nanorods doped with P for rapid HER and OER, Kinetics, Small 20 (2024) 2305519, https://doi.org/10.1002/smll.202305519.

[4] P. Dong, T. Cheng, J. Zhang, J. Jiang, L. Zhang, X. Xi, J. Zhang, Fabrication of an organic/inorganic hybrid TpPa-1-COF/$ZnIn_2S_4$ S-scheme heterojunction for boosted photocatalytic hydrogen production, ACS Appl. Energy Mater. 6 (2023) 1103–1115, https://doi.org/10.1021/acsaem.2c03806.

[5] D. Ma, J. Chen, J. Li, X. Ji, J.-W. Shi, A review on passivation engineering for improving photocatalytic hydrogen evolution performance, J. Mater. Chem. A 12 (2024) 12293–12324, https://doi.org/10.1039/D4TA00411F.

[6] D. Ma, X. Zhang, C. Yang, X. Feng, Z.-F. Zhang, K. Song, S. Wu, L. Li, T. Jiang, J.-W. Shi, Insight into the role of Ni atoms at the interface of g-C_3N_4/CdS in photocatalytic H_2 evolution, Sep. Purif. Technol. 327 (2023) 124996, https://doi.org/10.1016/j.seppur.2023.124996.

[7] G. Sun, B. Xiao, J.-W. Shi, S. Mao, C. He, D. Ma, Y. Cheng, Hydrogen spillover effect induced by ascorbic acid in CdS/NiO core-shell p-n heterojunction for significantly enhanced photocatalytic H_2 evolution, J. Colloid Interface Sci. 596 (2021) 215–224, https://doi.org/10.1016/j.jcis.2021.03.150.

[8] X. Yu, H. Su, J. Zou, Q. Liu, L. Wang, H. Tang, Doping-induced metal–N active sites and bandgap engineering in graphitic carbon nitride for enhancing photocatalytic H_2 evolution performance, Chin. J. Catal. 43 (2022) 421–432, https://doi.org/10.1016/S1872-2067(21)63849-4.

[9] L. Sun, X. Yu, L. Tang, W. Wang, Q. Liu, Hollow dodecahedron $K_3PW_{12}O_{40}$/CdS core-shell S-scheme heterojunction for photocatalytic synergistic H_2 evolution and benzyl alcohol oxidation, Chin. J. Catal. 52 (2023) 164–175, https://doi.org/10.1016/S1872-2067(23)64507-3.

[10] W. Wang, S. Mei, H. Jiang, L. Wang, H. Tang, Q. Liu, Recent advances in TiO_2-based S-scheme heterojunction photocatalysts, Chin. J. Catal. 55 (2023) 137–158, https://doi.org/10.1016/S1872-2067(23)64551-6.

[11] H. Su, W. Wang, R. Shi, H. Tang, L. Sun, L. Wang, Q. Liu, T. Zhang, Recent advances in quantum dot catalysts for hydrogen evolution: synthesis, characterization, and photocatalytic application, Carbon Energy 5 (2023) e280, https://doi.org/10.1002/cey2.280.

[12] Q. Wang, K. Domen, Particulate photocatalysts for light-driven water splitting: mechanisms, challenges, and design strategies, Chem. Rev. 120 (2020) 919–985, https://doi.org/10.1021/acs.chemrev.9b00201.

[13] X. Chu, C.I. Sathish, J. Yang, X. Guan, X. Zhang, L. Qiao, K. Domen, S. Wang, A. Vinu, J. Yi, Strategies for improving the photocatalytic hydrogen evolution reaction of carbon nitride-based catalysts, Small 19 (2023), https://doi.org/10.1002/smll.202302875.

[14] Y. Li, L. Yang, H. He, L. Sun, H. Wang, X. Fang, Y. Zhao, D. Zheng, Y. Qi, Z. Li, W. Deng, In situ photodeposition of platinum clusters on a covalent organic framework for photocatalytic hydrogen production, Nat. Commun. 13 (2022) 1355, https://doi.org/10.1038/s41467-022-29076-z.

[15] H. Jin, X. Liu, S. Chen, A. Vasileff, L. Li, Y. Jiao, L. Song, Y. Zheng, S.-Z. Qiao, Heteroatom-doped transition metal electrocatalysts for hydrogen evolution reaction, ACS Energy Lett. 4 (2019) 805–810, https://doi.org/10.1021/acsenergylett.9b00348.

[16] D. Strmcnik, M. Uchimura, C. Wang, R. Subbaraman, N. Danilovic, D. van der Vliet, A.P. Paulikas, V.R. Stamenkovic, N.M. Markovic, Improving the hydrogen oxidation reaction rate by promotion of hydroxyl adsorption, Nat. Chem. 5 (2013) 300–306, https://doi.org/10.1038/nchem.1574.

[17] A.Y. Faid, A.O. Barnett, F. Seland, S. Sunde, Ni/NiO nanosheets for alkaline hydrogen evolution reaction: in situ electrochemical-Raman study, Electrochim. Acta 361 (2020) 137040, https://doi.org/10.1016/j.electacta.2020.137040.

[18] J. Wang, S. Mao, Z. Liu, Z. Wei, H. Wang, Y. Chen, Y. Wang, Dominating role of Ni^0 on the Interface of Ni/NiO for enhanced hydrogen evolution reaction, ACS Appl. Mater. Interfaces 9 (2017) 7139–7147, https://doi.org/10.1021/acsami.6b15377.

[19] Y. Dong, J. Dang, W. Wang, S. Yin, Y. Wang, First-principles determination of active sites of Ni metal-based electrocatalysts for hydrogen evolution reaction, ACS Appl. Mater. Interfaces 10 (2018) 39624–39630, https://doi.org/10.1021/acsami.8b12573.

[20] A.G. Oshchepkov, A. Bonnefont, V.A. Saveleva, V. Papaefthimiou, S. Zafeiratos, S. N. Pronkin, V.N. Parmon, E.R. Savinova, Exploring the influence of the nickel oxide species on the kinetics of hydrogen electrode reactions in alkaline media, Top. Catal. 59 (2016) 1319–1331, https://doi.org/10.1007/s11244-016-0657-0.

[21] M. Gong, W. Zhou, M.-C. Tsai, J. Zhou, M. Guan, M.-C. Lin, B. Zhang, Y. Hu, D.-Y. Wang, J. Yang, S.J. Pennycook, B.-J. Hwang, H. Dai, Nanoscale nickel oxide/nickel heterostructures for active hydrogen evolution electrocatalysis, Nat. Commun. 5 (2014) 4695, https://doi.org/10.1038/ncomms5695.

[22] K. Khaja Mohaideen, P.A. Joy, Influence of initial particle size on the magnetostriction of sintered cobalt ferrite derived from nanocrystalline powders, J. Magn. Magn. Mater. 346 (2013) 96–102, https://doi.org/10.1016/j.jmmm.2013.07.016.

[23] N. Kikukawa, M. Takemori, Y. Nagano, M. Sugasawa, S. Kobayashi, Synthesis and magnetic properties of nanostructured spinel ferrites using a glycine–nitrate process, J. Magn. Magn. Mater. 284 (2004) 206–214, https://doi.org/10.1016/j.jmmm.2004.06.039.

[24] H.N. Po, N.M. Senozan, The Henderson-Hasselbalch equation: its history and limitations, J. Chem. Educ. 78 (2001) 1499, https://doi.org/10.1021/ed078p1499.

[25] S. Kumar, M. Regue, M.A. Isaacs, E. Freeman, S. Eslava, All-inorganic $CsPbBr_3$ nanocrystals: gram-scale mechanochemical synthesis and selective photocatalytic CO_2 reduction to methane, ACS Appl. Energy Mater. 3 (2020) 4509–4522, https://doi.org/10.1021/acsaem.0c00195.

[26] H. Lai, Q. Wu, J. Zhao, L. Shang, H. Li, R. Che, Z. Lyu, J. Xiong, L. Yang, X. Wang, Z. Hu, Mesostructured NiO/Ni composites for high-performance electrochemical energy storage, Energy Environ. Sci. 9 (2016) 2053–2060, https://doi.org/10.1039/C6EE00603E.

[27] B. Li, Z. Ma, X. Zhang, J. Xu, Y. Chen, X. Zhang, C. Zhu, NiO/Ni heterojunction on N-doped hollow carbon sphere with balanced dielectric loss for efficient microwave absorption, Small 19 (2023), https://doi.org/10.1002/smll.202207197.

[28] C. Zhang, L. Qian, K. Zhang, S. Yuan, J. Xiao, S. Wang, Hierarchical porous Ni/NiO core–shells with superior conductivity for electrochemical pseudo-capacitors and glucose sensors, J. Mater. Chem. A 3 (2015) 10519–10525, https://doi.org/10.1039/C5TA01071C.

[29] K.M. Kamal, R. Narayan, N. Chandran, S. Popović, M.A. Nazrulla, J. Kovač, N. Vrtovec, M. Bele, N. Hodnik, M.M. Kržmanc, B. Likozar, Synergistic enhancement of photocatalytic CO_2 reduction by plasmonic au nanoparticles on TiO_2 decorated N-graphene heterostructure catalyst for high selectivity methane production, Appl. Catal. B Environ. 307 (2022) 121181, https://doi.org/10.1016/j.apcatb.2022.121181.

[30] S. Adhikari, G. Madras, Role of Ni in hetero-architectured NiO/Ni composites for enhanced catalytic performance, Phys. Chem. Chem. Phys. 19 (2017) 13895–13908, https://doi.org/10.1039/C7CP01332A.

[31] M.A. Rahman, C. Wen, Nanogravel structured NiO/Ni foam as electrode for high-performance lithium-ion batteries, Ionics (Kiel). 21 (2015) 2709–2723, https://doi.org/10.1007/s11581-015-1475-2.

[32] N. Mironova-Ulmane, A. Kuzmin, I. Steins, J. Grabis, I. Sildos, M. Pärs, Raman scattering in nanosized nickel oxide NiO, J. Phys. Conf. Ser. 93 (2007) 012039, https://doi.org/10.1088/1742-6596/93/1/012039.

[33] N. Mironova-Ulmane, A. Kuzmin, I. Sildos, L. Puust, J. Grabis, Magnon and phonon excitations in Nanosized NiO, Latv. J. Phys. Tech. Sci. 56 (2019) 61–72, https://doi.org/10.2478/lpts-2019-0014.

[34] Y. Rao, X. Qi, Q. Peng, Y. Chen, X. Gong, R. Xie, W. Zhong, Flower-like NiO to flower-like NiO/Ni@C microspheres: an effective strategy to comprehensively improve the loss capabilities, J. Colloid Interface Sci. 629 (2023) 981–993, https://doi.org/10.1016/j.jcis.2022.09.027.

[35] A. Gandhi, S. Wu, Strong deep-level-emission photoluminescence in NiO nanoparticles, Nanomaterials 7 (2017) 231, https://doi.org/10.3390/nano7080231.

[36] J. Zhang, D. Zeng, Q. Zhu, J. Wu, Q. Huang, C. Xie, Effect of nickel vacancies on the room-temperature NO $_2$ sensing properties of mesoporous NiO Nanosheets, J. Phys. Chem. C 120 (2016) 3936–3945, https://doi.org/10.1021/acs.jpcc.5b12162.

[37] Y. Yang, S. Zhao, F. Bi, J. Chen, Y. Wang, L. Cui, J. Xu, X. Zhang, Highly efficient photothermal catalysis of toluene over Co_3O_4/TiO_2 p-n heterojunction: the crucial roles of interface defects and band structure, Appl. Catal. B Environ. 315 (2022) 121550, https://doi.org/10.1016/j.apcatb.2022.121550.

[38] F. Xing, C. Cheng, J. Zhang, Q. Liu, C. Chen, C. Huang, Tunable charge transfer efficiency in $HxMoO_3$@$ZnIn_2S_4$ hierarchical direct Z-scheme heterojunction toward efficient visible-light-driven hydrogen evolution, Appl. Catal. B Environ. 285 (2021) 119818, https://doi.org/10.1016/j.apcatb.2020.119818.

[39] Y. Huang, D. Li, Z. Fang, R. Chen, B. Luo, W. Shi, Controlling carbon self-doping site of g-C_3N_4 for highly enhanced visible-light-driven hydrogen evolution, Appl. Catal. B Environ. 254 (2019) 128–134, https://doi.org/10.1016/j.apcatb.2019.04.082.

[40] M.S. Nasir, G. Yang, I. Ayub, S. Wang, W. Yan, Tin diselinide a stable co-catalyst coupled with branched TiO_2 fiber and g-C_3N_4 quantum dots for photocatalytic hydrogen evolution, Appl. Catal. B Environ. 270 (2020) 118900, https://doi.org/10.1016/j.apcatb.2020.118900.

[41] C. Boerigter, U. Aslam, S. Linic, Mechanism of charge transfer from Plasmonic nanostructures to chemically attached materials, ACS Nano 10 (2016) 6108–6115, https://doi.org/10.1021/acsnano.6b01846.

[42] J. Wang, Q. Yao, C. Huang, X. Zou, L. Liao, S. Chen, Z. Fan, K. Zhang, W. Wu, X. Xiao, C. Jiang, W. Wu, High mobility MoS_2 transistor with low Schottky barrier contact by using atomic thick h-BN as a tunneling layer, Adv. Mater. 28 (2016) 8302–8308, https://doi.org/10.1002/adma.201602757.

[43] K.A. Davis, S. Yoo, E.W. Shuler, B.D. Sherman, S. Lee, G. Leem, Photocatalytic hydrogen evolution from biomass conversion, Nano Converg. 8 (2021) 6, https://doi.org/10.1186/s40580-021-00256-9.

[44] L. Liu, S. Du, X. Guo, Y. Xiao, Z. Yin, N. Yang, Y. Bao, X. Zhu, S. Jin, Z. Feng, F. Zhang, Water-stable nickel metal–organic framework nanobelts for cocatalyst-free photocatalytic water splitting to produce hydrogen, J. Am. Chem. Soc. 144 (2022) 2747–2754, https://doi.org/10.1021/jacs.1c12179.